First observations of the Kr multi-monochromatic X-ray imager in OMEGA implosion experiments

E. Gallardo-Diaz,[1] R. C. Mancini,[1] J. Clapp,[1] P. Adrian,[2] T. E. Evans,[2] J. Frenje,[2] R. Florido,[3] V. A. Kruse,[4] T. Nagayama,[5] and D. T. Bishel[6]

[1)] *Physics Department, University of Nevada, Reno, 89557, NV, USA*

[2)] *Plasma Science Fusion Center, Massachusetts Institute of Technology, 02139, MA, USA*

[3)] *iUNAT-Departamento de Física, Universidad de Las Palmas de Gran Canaria, 35017, Las Palmas de Gran Canaria, Spain*

[4)] *Lawrence Livermore National Laboratories, P.O. Box 808, Livermore, 94550, CA, USA*

[5)] *Sandia National Laboratories, 1611 Innovation Pkwy SE, Albuquerque, 87123, NM, USA*

[6)] *Laboratory for Laser Energetics, University of Rochester, Rochester, 14623-1299, NY , USA*

(*Electronic mail: enacgallardo@nevada.unr.edu)

(Dated: 6 March 2024)

ABSTRACT

This paper presents initial findings from the recently deployed Kr Multi-Monochromatic X-ray Imager (MMI) at the Omega facility. The experiment focuses on exploring implosion dynamics in exploding pusher capsules at three distinct initial gas fill densities. Utilizing time-gated and spatially integrated measurements, core size, electron temperature (T_e), and electron densities (n_e) are derived through the analysis of the spectral region encompassing the Kr Heα and its satellite lines. A comprehensive spectral database, incorporating atomic kinetics, radiation transport, and Stark broadening, has been developed for rigorous data analysis. These measurements underscore the utility of the new Kr MMI instrument, enabling the diagnosis of plasma conditions at $T_e > 2000$ eV, thereby extending the capabilities beyond the prior Ar MMI design.

I. INTRODUCTION

High Energy Density Physics (HEDP) constitutes an interdisciplinary field dedicated to examining the behavior of matter in a plasma state, characterized by a broad spectrum of high temperatures and densities. A primary method for generating such extreme states involves direct drive Inertial Confinement Fusion (ICF) experiments. In this approach, high-power laser beams are directed in a spherically symmetric configuration towards a millimeter-scale spherical capsule. This capsule, comprised of a shell and gas fill containing fusion reactants, undergoes laser-induced ablation on its outer surface. Consequently, the inner shell functions as a piston, compelling the gas fill to compress. This implosion results in an increase of the gas density and temperature, creating a plasma state where the fusion reactions are held. ICF-type implosions are also employed as experimental platforms to perform basic high-energy density science to study, for example, ion stopping power[1] and electron-ion energy transfer and thermalization. However, these implosion core plasmas exist within a highly confined region of both space ($\sim \mu m$) and time ($\sim ns$) before the system undergoes expansion and cooling. Due to the plasma's extreme conditions, these systems prove challenging to diagnose and study. Essential parameters for understanding the ongoing processes within the plasma are its temperature and density. In this context, X-ray spectroscopy has emerged as a powerful technique to diagnose conditions within implosion cores[2–16].

X-ray spectroscopy serves as a valuable technique for diagnosing the electron temperature (T_e) and density (n_e) of plasma by leveraging the characteristic spectral signature of a spectroscopic tracer embedded in the gas fill of the capsule. The emitted spectra of this tracer must exhibit sensitivity to T_e and n_e within the anticipated diagnostic ranges. Employing collisional-radiative atomic kinetic models, detailed spectral line shapes and spectroscopic-quality radiation transport one can calculate the sensitivity of the spectra with the plasma conditions, enabling a comparison with the experimental data.

Historically, the use of argon K-shell (photon energy 3-4.5 keV) has been prevalent as a spectroscopic tracer for diagnosing core T_e and n_e[2–10,16]. However, the usefulness of the Ar K-shell spectrum diminishes significantly for T_e values exceeding 2000 eV due to the increasing ionization of electronic states responsible for these line transitions. To address the need for diagnosing these hot plasmas at T_e values surpassing 2000 eV, a higher-Z spectroscopic tracer becomes imperative. Kr, as the higher-Z noble gas succeeding Ar, emerges as an attractive alternative. Previous studies have demonstrated the utility of Kr K-shell (13-16 keV) in diagnosing hot implosion cores at the National Ignition Facility (NIF)[13–15,17,18]. Additionally, the Kr L-shell spectrum (2.7-3.5 keV) has exhibited sensitivity to Te in the range of 1500 to 3000 eV[19].

In this research we add a tracer concentration of Kr to the gas fill and use the K-shell emission to diagnose T_e and n_e in hot (T_e>2000 eV) implosion core experiments at the Omega Laser Facility. The shell of the capsules is made of Hoppe glass and the gas fill contains a mixture of D_2, ^{3}He and tracer amounts of T and Kr. In order to detect the Kr K-shell line emission we use two spectrometers: XRS and a recently developed instrument known as the krypton Multi-Monochromatic X-ray Instrument (Kr MMI).

This publication emphasizes spatially integrated measure-

ments of the Kr MMI, specifically analyzing the core sizes from the Heα spectral region and comparing the results with corresponding XRS measurements. In addition, we discuss the spectroscopic modeling employed and demonstrate our analysis method for extracting plasma conditions from spectroscopic data.

This paper is organized as follows: Section II describes the experimental setup used in these campaigns focusing on the Kr MMI instrument. Section III compares the core size measurements extracted from XRS and Kr MMI data. Next, Section IV discusses the model employed to develop the spectral database. Furthermore, this section shows the analysis method used to extract plasma conditions from the experimental measurements. Finally, Section V summarises the conclusions of this research.

II. KR MMI AND EXPERIMENTAL SETUP

The original design of the MMI was tailored to detect photon energy ranges corresponding to the Ar and Ti K-shell (3-6 keV). This version has found extensive application at Omega, facilitating the diagnosis of both shell[20–26] and core conditions[1,20,27–34]. The need to utilize Kr K-shell for diagnosing plasma conditions in hot implosion cores prompted a modification of the instrument to capture the corresponding photon energy range (12-16 keV). The design details of the Kr MMI are documented in a previous publication[35].

The Kr MMI employs a Pinhole Array (PHA) to image the plasma, and these images are subsequently dispersed by a flat Ge(220) crystal into a time-gated Micro-Channel Plate (MCP) detector. This diagnostic capability is particularly powerful, as it provides spectra with 2D spatial resolution at four gated times. The characteristic feature of the MMI instrument is that it records gated arrays of spectrally resolved images. From these data narrow- and broad-band images as well as spatially integrated and resolved spectra can be extracted[16,21]. From this dataset, we can extract distributions of T_e and n_e in the core and observe their temporal evolution. These results offer valuable insights into implosion physics, including electron thermal transport and energy balance.

A refinement has been implemented in the Kr MMI design with respect to the one outlined in the preceding publication[35]. To improve the instrument performance, a specific adjustment has been made to the position of the PHA, denoted as Zpha in Ref. [35], shifting it from -1.2 to -1.29 mm. Additionally, the PHA height, represented by Hpha, has been reduced from 2.323 to 2.144 mm. These alterations ensure that all incident light entering the spectrometer undergoes reflection off the crystal within the system. Furthermore, the inner radius of the cylindrical nose has been augmented to prevent any potential clipping on its inner surface.

As of November 2023, the Kr MMI has been fielded in three distinct Omega campaigns, yielding successful and valuable data. The different experiments explored different regions in parameter space varying laser energy, gas fill pressure and shell thickness. However, this paper will focus on the third campaign conducted in August 2023 as it was the first one to use 4 time gated MCP measurements and the first one that collected Heβ data due to the high T_e achieved.

The experimental setup involves the utilization of a 1 ns square laser pulse with an energy output of 25 kJ. The capsule employed features 6 μm thick Hoppe glass shell. Variations in the gas fill pressure were introduced, with values set at 20, 11, and 7 atm. The gas mixture consisted of approximately 90% D_2, 10% ^{3}He, and trace amounts of T_2 and Kr, specifically at 0.01 atm each. To characterize the resulting plasma, a combination of X-ray and particle diagnostics was employed, with a particular emphasis on X-ray diagnostics as the focal point of this paper.

In these experiments, the XRS was fielded to both compare the findings obtained with the Kr MMI system. The XRS is a flat crystal spectrometer capable of generating 1D spatially resolved spectra when employed in conjunction with a slit. For detection in the Kr K-shell region, a Ge (111) crystal was utilized, along with a 25 μm slit and an image plate as detector. It is important to note a distinction from the Kr MMI: the XRS instrument operates on a temporally integrated basis. Consequently, the data generated by this instrument provides information on the temporally averaged conditions of the implosion, in contrast to the time-gated data obtained from the Kr MMI.

Figure 1 provides a visual representation of the spatial resolution difference between the two spectrometers. The XRS instrument's employment of a slit enables the resolution of one spatial dimension by integrating across a disk of thickness defined by the instrument's spatial resolution. Conversely, the Kr MMI, utilizing pinholes, resolves two spatial dimensions by integrating along a chord with a finite cross-section, restricted by the instrument's spatial resolution. To quantify the spatial resolution of the instruments including diffraction effects, we followed the methodology detailed in the Kr MMI design paper[35] and in Ref. [36]. The estimated spatial resolution for the MMI, employing 13 μm diameter pinholes, is approximately 20.8 μm at 13 keV.

In Figure 2, examples of data from both the XRS and MMI after correcting for their respective filter and detector response are presented. The MMI data displays one of the four time-gated frames, while the XRS data shows time integrated measurements. Both sets of images depict the emission regions of Kr Heα and Heβ. While the vertical axis serves as a spatial reference in both cases, the horizontal axis takes on different roles. For XRS, it denotes the spectral axis. In contrast, for MMI, this axis encompasses spatial, spectral, and temporal dimensions. The temporal dimension arises from the pulse sweep of the MCP strip, moving from left to right across the image to detect the signal at different moments in time.

III. CORE SIZE ANALYSIS

The spatial resolution provided by both XRS and MMI enables the estimation of the core size defined here as size of the Kr K-shell line emission region. This diameter represents the spherical core volume with sufficient temperature to ionize Kr and populate the upper energy levels of the 2-1 line transitions.

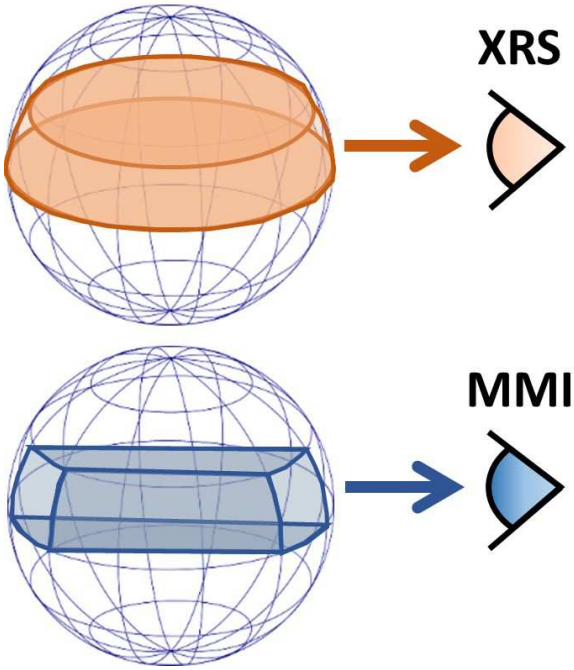

FIG. 1. Schematic representation illustrating the distinct volumes of integration for X-ray Spectrometer (XRS) and Multi-Monochromatic Imaging (MMI) in a spherical plasma. The XRS utilizes a slit, enabling the resolution of one spatial dimension by integrating over the emitted light within a disk limited by the instrument's spatial resolution. In contrast, MMI employs pinholes, allowing the resolution of two spatial dimensions by integrating over a chord of finite cross-section, also constrained by the instrument's spatial resolution.

A forward reconstruction method utilizing the system's Point Spread Functions (PSF), as detailed in Ref. [36], is employed for this purpose. Equation 3.1 in this report outlines the image intensity profile in the detector plane, denoted as $I(r)$, as the convolution of the source profile $S(r)$ with the different PSFs of the system:

$$I(r) = S(r) * P_{geom}(r) * P_{diff}(r) * P_{bragg}(r) * P_{det}(r) \quad (1)$$

Figure 3 illustrates each PSF contributing to $I(r)$ in XRS. The geometric PSF is a rectangular function defined by the 25 μm slit aperture and instrument magnification. The detector, an image plate in this case, has a Gaussian PSF of 130 μm FWHM[37]. The Bragg PSF accounting for the effect of the Ge crystal is considered relatively minor leading to its neglect[36]. For diffraction contribution, the method and code from Ref. [36] are followed to calculate P_{diff} at 13 keV. In the near-field or Fresnel regime, as shown in Figure 3, diffraction effects produce an oscillatory pattern, which, however, does not survive convolution with the remaining PSFs. $S(r)$ is represented by a Gaussian function with a FWHM defining the core size.

The forward reconstruction algorithm employs an array of core sizes to generate a set of $I(r)$ profiles. This set is then compared to the XRS spatial lineouts of the Kr Heα emission region using χ^2 minimization to obtain the estimated core size and its uncertainty.

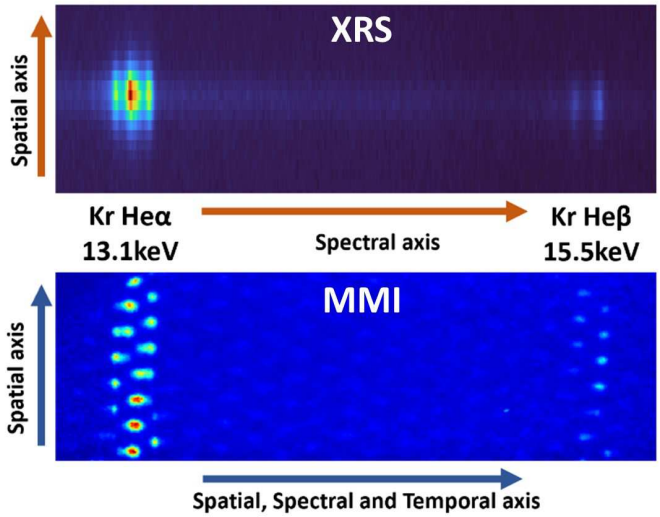

FIG. 2. XRS and MMI data after filter and detector response correction. Kr Heα and Heβ emission regions are labeled.

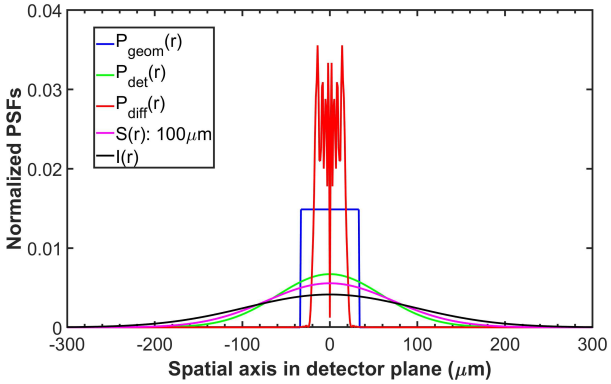

FIG. 3. Contributions to the final image intensity profile $I(r)$ formed in the detector plane for the case of XRS. $P_{geom}(r)$ represents the PSF of the 25μm slit. $P_{diff}(r)$ is the PSF contribution due to diffraction effects at 13 keV. $P_{det}(r)$ is the image plate PSF. The $S(r)$ source profile is represented by a Gaussian function which FWHM is defined as the core size. In this case we have used a core size of 100μm to illustrate the convolution.

For the Kr MMI, P_{geom} is defined by a 13 μm pinhole, and P_{det} is a 50 μm FWHM Gaussian function representing the MCP resolution[36]. Diffraction effects are considered by calculating P_{diff} for the Kr MMI system.

Figure 4 displays time-gated MMI (data points) and time-integrated XRS (broken lines) core size estimated using the forward reconstruction method for three different capsule fill pressures: 20, 11, and 7 atm. The solid line represents the linear fit to the MMI data points for each case. XRS measurements indicate a reduction in core size with decreasing initial pressure as detailed in Table I. This trend aligns with the expectation of decreased core compression resistance due to lower fuel pressure, as supported by 1-D hydrodynamic simulations performed with HYADES[38]. However, these simula-

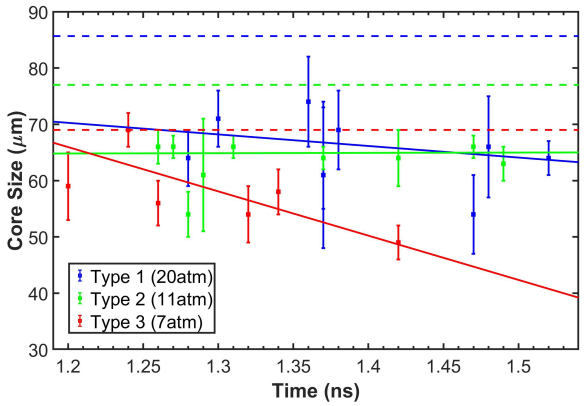

FIG. 4. MMI core size measurements (data points) and linear best fit trends (solid lines) for the three different initial pressures. XRS time integrated core sizes are also represented (broken lines) and present an uncertainty of $\pm$ 4 μm.

tions underpredict the core size at lower initial pressures.

TABLE I. Core size from XRS time integrated measurements and HYADES hydrodynamic simulations.

Initial Pressue (atm)	XRS (μm)	Hydro simulation (μm)
20	86$\pm$4	88
11	77$\pm$4	56
7	69$\pm$4	40

MMI measurements enable the study of the time evolution of the core size between 1.2 and 1.52 ns relative to the leading laser pulse. The data illustrates the decreasing trend of core size with decreasing initial pressure. Additionally, the core size decreases with time for all cases except the 11 atm case, which shows a relatively constant diameter. The reduction in the size of the core region emitting the Kr Heα line with time suggests either ongoing compression, cooling of the core, or a combination of both.

Comparing XRS and MMI core sizes reveals that time-gated measurements are consistently smaller than time-integrated ones. This suggests a period during the implosion, likely preceding the gated measurements at 1.2 ns, where the size of the region emitting the Kr line was larger than that measured during this specific time window.

IV. SPECTROSCOPIC ANALYSIS

A detailed spectral database was developed by combining results from diverse models. PrismSpect[39] was employed for modeling the plasma atomic kinetics, yielding level populations for various combinations of T_e and n_e. FAC[40] was used to calculate line transition energies and rates. Additionally, MERL[41] was utilized for conducting detailed Stark broadening calculations of the line profiles. We choose to use FAC data rather than PrismSpect's internal atomic database (ATBASE) as it better approximates the experimental Kr Heα satellite line emission photon energies.

Emissivity ($j(h\nu)$) and opacity ($k(h\nu)$) profiles are computed using the following equations[19]:

$$j(h\nu) = \sum_{\alpha\beta} \frac{h\nu}{4\pi} N_\beta A_{\beta\alpha} \Phi_{\alpha\beta}(h\nu) \tag{2}$$

$$k(h\nu) = \sum_{\alpha\beta} \frac{h\nu}{4\pi} (N_\alpha B_{\alpha\beta} - N_\beta B_{\beta\alpha}) \Phi_{\alpha\beta}(h\nu) \tag{3}$$

Where α and β represent the lower and upper states of each transition respectively. N_α is the population of α level, $\Phi_{\alpha\beta}(h\nu)$ is the line profile and $A_{\alpha\beta}$ and $B_{\alpha\beta}$ are the Einstein coefficients of the transition from state α to state β.

In our database, the populations (N) are derived from PrismSpect output, while the coefficients (A and B) are determined through FAC. The line profiles ($\Phi_{\alpha\beta}(h\nu)$) are computed using MERL, incorporating FAC transition energies.

PrismSpect calculations were conducted using the Kr atomic model outlined in our previous study of the Kr L-shell region[19] which is detailed in Table 2 of Ref. [42]. The former reference demonstrates a notable agreement in the plasma Charge State Distribution (CSD) between PrismSpect and ABAKO[43] calculations. The simulations in the current paper maintained a non-LTE approach, with radiation transport being solved inline with atomic kinetic equations tailored for a spherical plasma with a diameter of 94 μm. This diameter was determined as an effective average, considering the core sizes of the current campaign and slightly larger ones from previous experiments.

The methodology employed to calculate the line shapes of Kr Heα and its satellites follows the approach outlined in a prior study concerning the Stark broadening effect on Heβ and its accompanying satellites[44]. MERL simulations employed APEX[45] to compute the plasma microfield distribution at various n_e. Line profiles were calculated based on the standard Stark-broadening theory approximation[46], assuming static ions and dynamic electrons. Specifically, for Kr Heα and its satellites, the line profiles considered encompassed the Kr Heα resonance and intercombination line, along with Li-like n=2, 3, and 4 satellites, and Be-like n=2 satellites. PrismSpect level population data served as input for these calculations.

Figure 5 illustrates the total emissivity $j(h\nu)$ computed from Eq. 2 for $T_e = 2000$ eV and n_e=10^{24}/cc, alongside the contribution from the different line shapes considered. This plot shows the complexity of this spectral region due to the overlap among the contributions of the different ions. It is worth noting that the Heα resonance line becomes optically thick (Optical depth ≥ 1) for many of the n_e values considered in our model.

Following the methodology outlined in a previous paper[19], $j(h\nu)$ and $k(h\nu)$ were utilized to compute the Emergent Intensity Distribution (EID) of a uniform sphere[47]. The resultant EID, generated for various combinations of T_e and n_e,

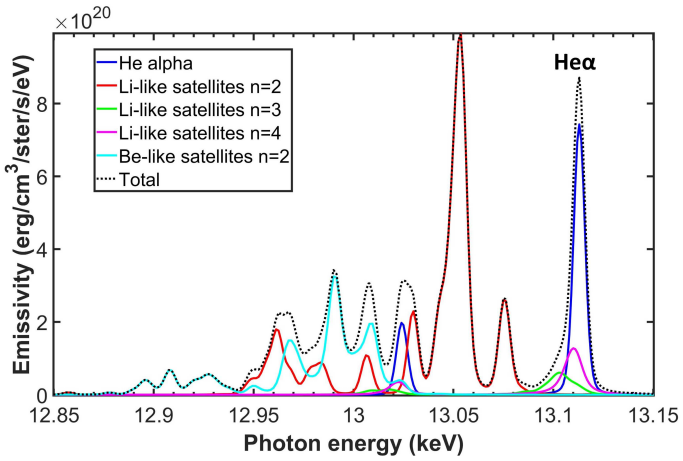

FIG. 5. Kr Heα emissivity and line shape contribution for $T_e = 2000$ eV and n_e=10^{24}/cc.

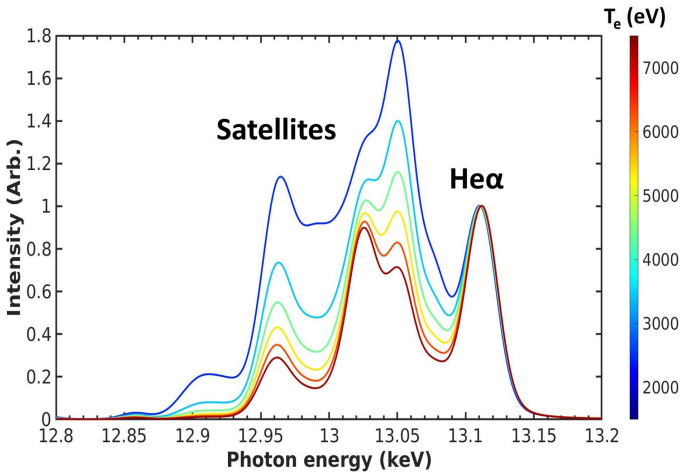

FIG. 6. Kr Heα Emergent Intensity Distribution T_e sensitivity at n_e=10^{24}/cc. The spectra contains contributions from the Kr Heα resonance and intercombination line, the Li-like n=2, 3 and 4 satellites and Be-like n=2 satellites. This case is for a 94μm diameter core and convolved with a 21.9eV Gaussian function to account for the MMI spectral resolution.

formed a spectral database. Subsequently, convolution with a Gaussian function, characterized by a FWHM corresponding to the spectral resolution of each instrument, was performed. This facilitated the implementation of Bayesian analysis to estimate the plasma conditions.

Figures 6 and 7 depict the sensitivity of the EID with respect to T_e and n_e, respectively. In these figures, the EID is convolved with a 21.9 eV FWHM Gaussian, representing the MMI spectral resolution. All traces are normalized to the Heα resonance line for comparative analysis.

In Figure 6, the ionization of lower charged states leading to satellite lines (Be- and Li-like) is evident with increasing T_e. The relative emission between the Heα and the satellite lines proves sensitivity to T_e within the 1500-6500 eV range.

Figure 7 illustrates the sensitivity of the line profiles with

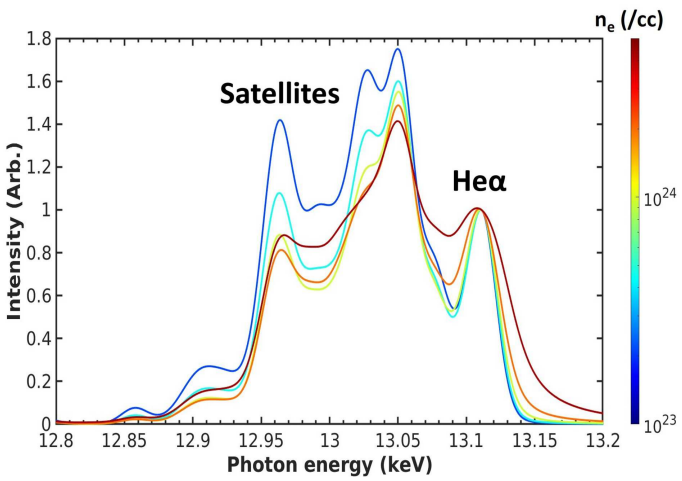

FIG. 7. Kr Heα Emergent Intensity Distribution n_e sensitivity at T_e=3000eV. The spectra contains contributions from the Kr Heα resonance and intercombination line, the Li-like n=2, 3 and 4 satellites and Be-like n=2 satellites. This case is for a 94μm diameter core and convolved with a 21.9eV Gaussian function to account for the MMI spectral resolution.

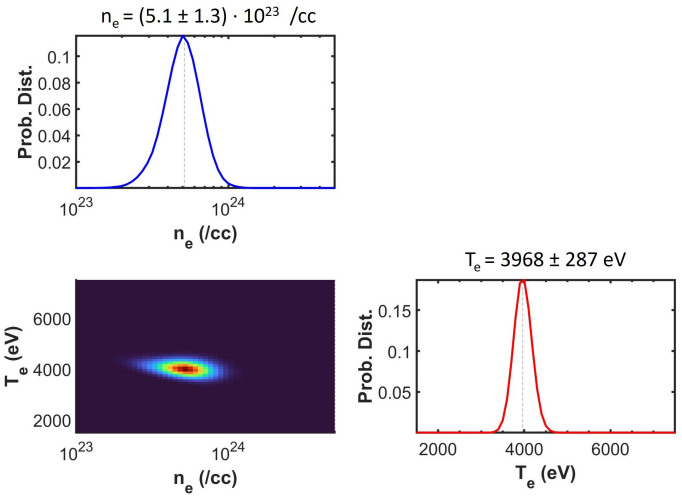

FIG. 8. Corner plot displaying the posterior probability distribution function for the spatially integrated data from frame number 2 of shot s109486 in the MMI dataset (P=20 atm, t=1.33 ns). The color map represents the posterior probability distribution in parameter space, with red representing the maximum value. The top and right plots presents the marginalized distributions for n_e and T_e, respectively. The dashed vertical line indicates the expected value. The titles of both plots specify the estimated values of n_e and T_e, along with their uncertainties derived from the FWHM of the distributions.

n_e. The change in the spectra is a result of the dependence of the atomic kinetics and the Stark broadening effect with n_e. Particularly, the impact of Stark broadening is prominently observed in the fill of the valley between the Heα resonance line and the primary Li-like satellite line.

We performed Bayesian analysis where the posterior probability distribution is defined as[48]:

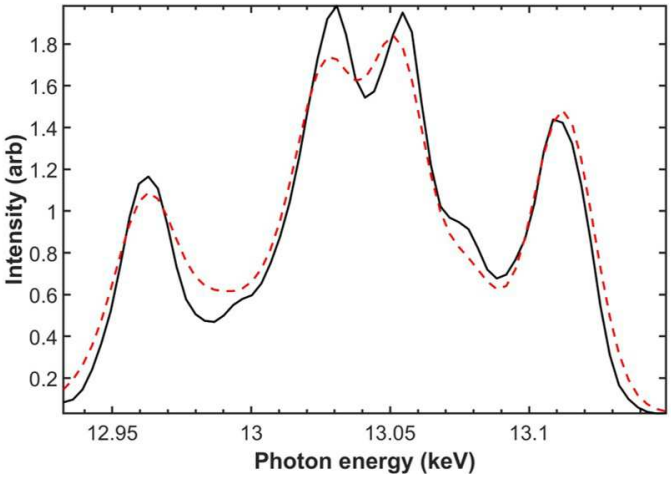

FIG. 9. Experimental spatially integrated spectrum (black solid) and best fit (red dashed) for MMI frame 2 data from s109486. The best fit corresponds to the theoretical spectrum with $T_e = 3968$ eV and $n_e = 5.1 \cdot 10^{23}$/cc as shown in figure 8.

$$P(T_e, n_e | y_1, y_2, \dots) = \frac{P(y_1, y_2 \dots | T_e, n_e)\, P(T_e, n_e)}{P(y_1, y_2, \dots)} \quad (4)$$

In this equation, y_i are the individual recorded intensities for each of the N data points that form the spectrum. $P(T_e, n_e)$ corresponds to the prior probability distribution while $P(y_1, y_2, \dots)$ is the evidence or normalization factor of the posterior. The likelihood function $P(y_1, y_2, \dots | T_e, n_e)$ is defined as follows:

$$P(y_1, y_2, \dots | T_e, n_e) \equiv \prod_i^N \exp\left\{ -\frac{\left(y_i^{model}(T_e, n_e) - y_i\right)^2}{2\sigma_i^2} \right\} \quad (5)$$

Here, σ_i represent the statistical weights associated to the error of the measurement and $y_i^{model}(T_e, n_e)$ are the intensities calculated in the spectral database for the different combinations of T_e and n_e .

We assume uniform prior probability distribution $P(T_e, n_e)$ =const, which is appropriate when the likelihood function is non-zero only over finite parameter space. The sampling of likelihood function is typically done using Markov-Chain Monte Carlo (MCMC); however, in our case of application this technique is not necessary since we only count with two parameters (i.e., T_e and n_e). Thus, we can numerically evaluated the likelihood function exhaustively as function of T_e and n_e values.

Figure 8 illustrates the posterior distribution function for the MMI data in frame 2 from shot s109486. This shot corresponds to a type 1 shot with 20 atm initial pressure timed at 1.33 ns. The expected values of the T_e and n_e probability distribution functions represent the most probable conditions given our experimental data. Furthermore, the FWHM of the distribution corresponds to the uncertainty of this measurement.

Figure 9 displays the experimental data alongside the best fit obtained through the Bayesian analysis. The fit effectively captures the overall spectral shape for both the Heα line and its satellites. However, it does not accurately reproduce the relative intensity of the central double peak structure. From the analysis of this data, the extracted plasma conditions are $T_e = 3968$ eV and $n_e = 5.1 \cdot 10^{23}$/cc with uncertainties of 7% and 25% respectively which are typical for this type of analysis.

Future investigations will explore a comprehensive analysis of the results obtained through this technique, focusing on both the time integrated spectra from XRS and the time-gated MMI spatially integrated measurements. Furthermore, forthcoming work will include detailed data analysis of the MMI spatially resolved Heβ spectra, enabling the extraction of 2D maps depicting the spatial distribution of T_e and n_e. These findings will be presented in a subsequent publication.

V. CONCLUSIONS

This research marks a significant milestone with the introduction of the Kr MMI instrument at the Omega laser facility. The findings demonstrate the instrument's capability to yield electron temperature and density measurements in hot implosion cores (T_e > 2000 eV), a capability not attainable with the previous MMI version utilizing Ar as spectroscopic tracer. The focus of this paper centers on the core size analysis of XRS and MMI as well as the development of a spectroscopic model and analysis method to diagnose plasma conditions. To this end, we present the Bayesian analysis conducted on one of the time-gated spatially integrated MMI datasets. A subsequent publication will explore the time resolved spatially integrated Heα results and spatially resolved diagnostics analyzing the Heβ spectral region.

The analysis of MMI data has provided insights into the size of the Kr emission region, offering a comparative perspective with XRS time-integrated data. Time-gated measurements unveil a reduction in core size between 1.2 and 1.52 ns relative to the leading laser pulse. Contrastingly, time-integrated data indicates a larger core size than the time-gated MMI data, hinting at a larger size at earlier times. Both datasets reveal a decrease in core size with decreasing fill pressure, aligning with simulation expectations. However, simulations predict smaller core sizes at low fill pressures.

The development of a detailed Emergent Intensity Distribution (EID) database has facilitated precise diagnosis of plasma conditions from Kr spectra. The combination of different modeling codes results in a EID that exhibits sensitivity with T_e and n_e. Employing Bayesian analysis we obtain probability distributions for the plasma conditions, allowing for estimation of their most probable values and uncertainties. The best fit shows an overall good quality agreement with the experimental spectrum.

The new Kr MMI instrument emerges as a robust diagnostic tool which extends the capabilities of the previous Ar MMI, unlocking a new region in parameter space for time-gated and 2D spatially resolved spectroscopic measurements. The col-

lected data holds the potential to offer valuable insights into implosion dynamics and plasma distributions. The time and spatial resolution offered by this instrument provide a distinct advantage over other spectrometers that lack the ability to resolve all these dimensions, such as XRS. Currently, we are in the process of manufacturing two additional MMI designs to target different spectral regions of interest: the Cu K-shell (7.5-10 keV) and the Ge K-shell (9-12.5 keV) MMIs. These new designs will expand the range of tracers usable with this instrument, thereby enhancing its versatility.

ACKNOWLEDGMENTS

We wish to acknowledge the support of Dr. Tregillis regarding the estimation of the diffraction contribution to the instrumental spatial resolution. This work was supported in part by DOE/NNSA Cooperative Agreement Grant DE-NA0003868. Part of this work was performed under the auspices of the U.S. Department of Energy by Lawrence Livermore National Laboratory under Contract DE-AC52-07NA27344. This work has also been supported in part by Research Grants No. PID2022-137632OB-I00 from the Spanish Ministry of Science, Innovation and Universities.

....

DATA AVAILABILITY STATEMENT

The data that support the findings of this study are available from the corresponding author upon reasonable request.

[1]J. A. Frenje, R. Florido, and et al, Phys. Rev. Lett. **122**, 015002 (2019).
[2]C. F. Hooper Jr., D. P. Kilcrease, R. C. Mancini, L. A. Woltz, D. K. Bradley, P. A. Jaanimagi, and M. C. Richardson, Phys. Rev. Lett. **63**, 267–270 (1989).
[3]R. C. Mancini, J. Hooper, C. F., N. D. Delamater, A. Hauer, C. J. Keane, B. A. Hammel, and J. K. Nash, Review of Scientific Instruments **63**, 5119–5121 (1992).
[4]C. J. Keane, B. A. Hammel, D. R. Kania, J. D. Kilkenny, R. W. Lee, A. L. Osterheld, L. J. Suter, R. C. Mancini, J. Hooper, C. F., and N. D. Delamater, Physics of Fluids B: Plasma Physics **5**, 3328–3336 (1993).
[5]D. A. Haynes, D. T. Garber, C. F. Hooper, R. C. Mancini, Y. T. Lee, D. K. Bradley, J. Delettrez, R. Epstein, and P. A. Jaanimagi, Phys. Rev. E **53**, 1042–1050 (1996).
[6]R. Florido, R. C. Mancini, T. Nagayama, R. Tommasini, J. A. Delettrez, S. P. Regan, and B. Yaakobi, Review of Scientific Instruments **81**, 10E307 (2010), https://doi.org/10.1063/1.3479024.
[7]R. Florido, R. Mancini, T. Nagayama, R. Tommasini, J. Delettrez, S. Regan, V. Smalyuk, R. Rodríguez, and J. Gil, High Energy Density Physics **6**, 70–75 (2010).
[8]R. Florido, R. C. Mancini, T. Nagayama, R. Tommasini, J. A. Delettrez, S. P. Regan, and B. Yaakobi, Phys. Rev. E **83**, 066408 (2011).
[9]R. Florido, R. C. Mancini, T. Nagayama, R. Tommasini, J. A. Delettrez, and S. P. Regan, Physics of Plasmas **21**, 102709 (2014), https://doi.org/10.1063/1.4898329.
[10]R. Florido and R. C. Mancini, Journal of Physics B: Atomic, Molecular and Optical Physics **48**, 224006 (2015).
[11]S. P. Regan, J. A. Delettrez, R. Epstein, P. A. Jaanimagi, B. Yaakobi, V. A. Smalyuk, F. J. Marshall, D. D. Meyerhofer, W. Seka, D. A. Haynes, I. E. Golovkin, and C. F. Hooper, Physics of Plasmas **9**, 1357–1365 (2002), https://doi.org/10.1063/1.1456530.
[12]I. Golovkin, R. Mancini, S. Louis, Y. Ochi, K. Fujita, H. Nishimura, H. Shirga, N. Miyanaga, H. Azechi, R. Butzbach, I. Uschmann, E. Förster, J. Delettrez, J. Koch, R. W. Lee, and L. Klein, Phys. Rev. Lett. **88**, 045002 (2002).
[13]T. Ma, H. Chen, P. K. Patel, M. B. Schneider, M. A. Barrios, D. T. Casey, H.-K. Chung, B. A. Hammel, L. F. Berzak Hopkins, L. C. Jarrott, S. F. Khan, B. Lahmann, R. Nora, M. J. Rosenberg, A. Pak, S. P. Regan, H. A. Scott, H. Sio, B. K. Spears, and C. R. Weber, Review of Scientific Instruments **87**, 11E327 (2016), https://aip.scitation.org/doi/pdf/10.1063/1.4960753.
[14]H. Chen, T. Ma, R. Nora, M. A. Barrios, H. A. Scott, M. B. Schneider, L. Berzak Hopkins, D. T. Casey, B. A. Hammel, L. C. Jarrott, O. L. Landen, P. K. Patel, M. J. Rosenberg, and B. K. Spears, Physics of Plasmas **24**, 072715 (2017), https://doi.org/10.1063/1.4993049.
[15]M. J. May, G. E. Kemp, J. D. Colvin, D. A. Liedahl, P. L. Poole, D. B. Thorn, K. Widmann, R. Benjamin, M. A. Barrios, and B. E. Blue, Physics of Plasmas **26**, 063105 (2019), https://doi.org/10.1063/1.5097960.
[16]T. Nagayama, R. C. Mancini, R. Florido, and et al, Physics of Plasmas **21**, 050702 (2014).
[17]L. Gao, B. F. Kraus, K. W. Hill, M. B. Schneider, A. Christopherson, B. Bachmann, M. Bitter, P. Efthimion, N. Pablant, R. Betti, C. Thomas, D. Thorn, A. G. MacPhee, S. Khan, R. Kauffman, D. Liedahl, H. Chen, D. Bradley, J. Kilkenny, B. Lahmann, E. Stambulchik, and Y. Maron, Phys. Rev. Lett. **128**, 185002 (2022).
[18]K. W. Hill, L. Gao, B. F. Kraus, M. Bitter, P. C. Efthimion, N. Pablant, M. B. Schneider, D. B. Thorn, H. Chen, R. L. Kauffman, D. A. Liedahl, M. J. MacDonald, A. G. MacPhee, H. A. Scott, S. Stoupin, R. Doron, E. Stambulchik, Y. Maron, and B. Lahmann, Plasma Physics and Controlled Fusion **64**, 105025 (2022).
[19]E. Gallardo-Diaz, R. Mancini, K. Carpenter, P. Adrian, J. Frenje, and R. Florido, "Temperature and density dependence of kr l-shell spectrum in hot dense plasmas," Physics of Plasmas - submitted for publication (2024).
[20]N. Izumi, T. W. Barbee, and et al, Review of Scientific Instruments **77**, 083504 (2006), https://doi.org/10.1063/1.2336194.
[21]R. C. Mancini, H. M. Johns, and et al, Physics of Plasmas **21**, 122704 (2014), https://doi.org/10.1063/1.4903324.
[22]J. A. Baumgaertel, P. A. Bradley, and et al, Physics of Plasmas **21**, 052706 (2014), https://doi.org/10.1063/1.4881463.
[23]R. C. Shah, B. M. Haines, and et al, Phys. Rev. Lett. **118**, 135001 (2017).
[24]B. Yaakobi, F. J. Marshall, and et al, Appl. Opt. **37**, 8074–8080 (1998).
[25]H. M. Johns, R. C. Mancini, and et al, Physics of Plasmas **21**, 082711 (2014), https://doi.org/10.1063/1.4892554.
[26]H. M. Johns, R. C. Mancini, and et al, Physics of Plasmas **23**, 012709 (2016), https://doi.org/10.1063/1.4940672.
[27]L. A. Welser, R. C. Mancini, and et al, **74**, 1951–1953 (2003), https://doi.org/10.1063/1.1535278.
[28]R. Tommasini, J. A. Koch, and et al, Review of Scientific Instruments **77**, 10E303 (2006), https://doi.org/10.1063/1.2218856.
[29]D. T. Cliche and R. C. Mancini, Appl. Opt. **58**, 4753–4761 (2019).
[30]J. A. Koch, T. W. Barbee, and et al, Review of Scientific Instruments **76**, 073708 (2005), https://doi.org/10.1063/1.1940614.
[31]S. Laffite, J. L. Bourgade, and et al, Physics of Plasmas **23**, 012706 (2016), https://doi.org/10.1063/1.4939833.
[32]T. R. Joshi, P. Hakel, and et al, Physics of Plasmas **24**, 056305 (2017), https://doi.org/10.1063/1.4978887.
[33]T. R. Joshi, S. C. Hsu, and et al, Physics of Plasmas **26**, 062702 (2019), https://doi.org/10.1063/1.5092998.
[34]S. C. Hsu, T. R. Joshi, and et al, EPL (Europhysics Letters) **115**, 65001 (2016).
[35]E. Gallardo-Diaz, R. C. Mancini, D. T. Cliche, and R. Tommasini, Review of Scientific Instruments **93**, 113525 (2022).
[36]I. L. Tregillis, LA-UR-16-27264 (2016), 10.2172/1327995.
[37]J. F. Seely, G. E. Holland, L. T. Hudson, and A. Henins, Appl. Opt. **47**, 5753–5761 (2008).
[38]J. T. Larsen and S. M. Lane, Journal of Quantitative Spectroscopy and Radiative Transfer **51**, 179–186 (1994), special Issue Radiative Properties of Hot Dense Matter.
[39]J. J. MacFarlane, Int. Fusion Science and Applications Conference Proceedings (2003).
[40]M. F. Gu, Canadian Journal of Physics **86**, 675–689 (2008), https://doi.org/10.1139/p07-197.

[41] R. Mancini, D. Kilcrease, L. Woltz, and C. Hooper, Computer Physics Communications **63**, 314–322 (1991).
[42] R. Florido, R. Rodríguez, J. M. Gil, J. G. Rubiano, P. Martel, E. Mínguez, and R. C. Mancini, Phys. Rev. E **80**, 056402 (2009).
[43] R. Florido, R. Rodríguez, J. M. Gil, J. G. Rubiano, P. Martel, E. Mínguez, and R. C. Mancini, Phys. Rev. E **80**, 056402 (2009).
[44] E. Gallardo-Diaz, R. C. Mancini, J. T. Clapp, and M. Kruse, "Krypton he line spectrum including n = 2, 3 li-like satellites with detailed stark broadened line shapes," High Energy Density Physics , 101081 (2024).
[45] C. Iglesias, F. Rogers, R. Shepherd, A. Bar-Shalom, M. Murillo, D. Kilcrease, A. Calisti, and R. Lee, Journal of Quantitative Spectroscopy and Radiative Transfer **65**, 303–315 (2000).
[46] B. Henry and H. Hora, Optics Communications **44**, 185–187 (1983).
[47] T. Burris-Mog, R. Mancini, J. Bailey, G. Chandler, G. Rochau, G. Dunham, P. Lake, K. Peterson, S. Slutz, T. Mehlhorn, I. Golovkin, and J. MacFarlane, Journal of Quantitative Spectroscopy and Radiative Transfer **99**, 120–130 (2006), radiative Properties of Hot Dense Matter.
[48] P. F. Knapp and W. E. Lewis, "Advanced data analysis in inertial confinement fusion and high energy density physics," Review of Scientific Instruments **94**, 061103 (2023)